



Experimental set-up of a thermal vacuum chamber for thermal model in-house correlation and characterization of the HYPSONO hyperspectral imager

Fermin Navarro-Medina¹ · Adrienne Esmeralda Oudijk² · Marie Bøe Henriksen² · Amund Gjersvik³ · Fredrik Sommerfelt Grønvold² · Tor Arne Johansen²

Received: 19 December 2022 / Revised: 19 April 2023 / Accepted: 20 April 2023

© The Author(s) 2023

Abstract

Space environment with changing temperatures and vacuum can affect the performance of optics instruments onboard satellites. Thermal models and tests are typically done to understand the optics performance within large space projects, but less often in nanosatellites projects. It is even more rarer for an optics payload inside a CubeSat platform, made by a third provider, to do functional tests on their optics during space environment test campaign. In this research, an in-house made vacuum chamber with the possibility to warm up (TVAC) the devices under tests, and wall-through transparency for optics experiments is set-up. In parallel, a thermal model of the HYPerspectral Small satellite for ocean Observation (HYPSONO) Hyperspectral Imager (HSI) is developed. The HSI, which is a transmissive grating hyperspectral instrument ranged in the visible to near infrared wavelength, has been tested in TVAC. As thermal control is based on heating the device under test, a new method for fitting the thermal models inside vacuum chambers with only heating capability is proposed. Finally, the TVAC set-up and the thermal model fitting method have been demonstrated to be appropriate to validate the HSI thermal model, and to characterize the optics performance of HSI in vacuum and in the range of temperatures found inside the in-orbit HYPSONO-1 CubeSat.

Keywords Vacuum thermal chamber · Thermal model · Hyperspectral camera · Thermal correlation

1 Introduction

Since first space exploration by optical instruments onboard spacecrafts, evidence exists that their optical performance depends significantly on the temperature variations in time and temperature gradients along the spatial position [1]. Modeling or testing this influence is not a simple problem, as it requires the combination of three main disciplines, i.e., thermal, structural, and optical design. Thermoelastic

models of optical instruments onboard spacecraft can be found in Refs. [2, 3], or [4]. More recently, an exhaustive study of the modeling procedure between the thermal and the structural models can be found in Ref. [5]. They highlight the relevance of the thermal and structural model qualities for the thermo-elastic results obtained. Tests to validate the design and the models are also fundamental, which is the focus of this paper.

The HYPerspectral Small satellite for ocean Observation (HYPSONO) Hyperspectral Imager (HSI) is a transmissive grating hyperspectral instrument ranged in the visible to near infrared wavelength [6]. The full range on the sensor spans from about 300 to 900 nm, as shown and discussed in Ref. [7], however, the 400 to 800 nm range is normally used. The HSI has a theoretical Full Width at Half-Maximum (FWHM) of 3.33 nm, and 124 spectral bands in the normal spectral range. The imager is the primary payload on the missions HYPSONO-1 (in-orbit since January 2022) and HYPSONO-2 (launch planned in 2024) [8]. HYPSONO-1 and 2 are a series of two 6U ocean color observation CubeSats

✉ Fermin Navarro-Medina
fermin.navarro.medina@uvigo.gal

¹atlanTTic, Universidade de Vigo, Escola de Enxeñaría Aeronáutica e do Espazo, Aerospace Technology Research Group, 32004 Ourense, Spain

²Department of Engineering Cybernetics, Norwegian University of Science and Technology, 7034 Trondheim, Norway

³Department of Electronic Systems, Norwegian University of Science and Technology, 7034 Trondheim, Norway

developed at the Norwegian University of Science and Technology (NTNU) [9]. HYPSON-1 has temperature sensors on the battery packs, the electric power system, and on the inside of the camera sensor of the HSI. The temperatures measured inside the camera sensor are typically in the range of 10–20 °C, depending on the orientation HYPSON-1 to the sun. During nominal image acquisition, the sensor is turned on for approximately 43 s, and the temperature increase in the HSI sensor is about 5 °C, due to more power dissipation from the electronics when acquiring images (and also due to the incoming radiation from the Earth). Typically, 5–6 images are acquired per day [8], with at least 1.5 h in between which allows for some cooling between image acquisitions. However, for HYPSON-2, it is planned to increase the image acquisition frequency and/or time, which will increase the temperature during operations. Therefore, some initial tests are also performed with HYPSON-1 with increased image acquisition time to investigate this temperature increase. As the temperature is only expected to increase, we focus on constructing an experimental vacuum chamber set-up that can be used to investigate the effect of increasing temperatures on the engineering model of the HSI, rather than effects from decreasing temperatures. One of the requirements for the set-up is also that it must be able to be used for low-cost space projects, and the set-up is therefore not made to be more complicated than necessary.

Thermal vacuum tests for spacecraft and space components are mandatory to demonstrate the feasibility of a system to be launched to space. Complete descriptions of thermal vacuum test campaigns for spacecrafts, even for small satellites, can be found in many references, e.g., Refs. [10, 11]. A smaller number of publications can be found regarding the design of thermal vacuum chambers. A review of spacecraft environment test technology was made in Ref. [12], including the thermal vacuum chambers. In spite of that the main concept of a vacuum chamber could be simple (sealed chamber and vacuum pumps), the addition of some thermal control inside, and the control of the test system itself adds some complexity. An example of a control system for spacecraft vacuum thermal test can be found in Ref. [13]. Thermal models of spacecraft may consider external planetary fluxes (IR and albedo) and direct solar flux. One of the main features of space is the harshness and variability of the thermal environment. This typically leads to large spatial and temporal temperature gradients within a space structure, which can range from several tens to hundreds of degrees Celsius [14]. An overview of the external heat fluxes on satellites is given in Ref. [15], and this can be carried over to a more accurate model describing heat transfer between satellite parts having different temperatures. The authors in Ref. [16] give an ANSYS example on how to model the thermal flow inside a camera. Reference [17] models the temperature ranges on the different parts of a satellite, including the

camera. Reference [18] shows the thermo-electric modeling of smallsats. Reference [19] made analytical study of thermal effects. Reference [20] presented a comparison of different paints in smallsats; and in Ref. [21], thermal load effects on satellite components are explained. All those papers provide partial information needed in our research.

Tests dedicated to thermal and thermo-elastic analysis within spacecraft missions typically include some types of temperature mapping and deformation measurement techniques. In Ref. [22], thermal imaging photogrammetry and ray-tracing scene modeling are combined in a 3D thermography system that can be used to validate thermal camera temperatures. This work could help us to guide the post-processing of the Infrared (IR) camera temperature maps, but the methodology used there is out of scope for a typical short CubeSat project. In Ref. [23], an assessment of the different technologies available to perform thermo-elastic distortion measurements has been performed. They explore the most suitable methodologies like photogrammetry and laser interferometry. In the same paper, the performance of a new photogrammetry method has been evaluated, which showed that the measurement points could be a priority parameter (even more relevant than the technique accuracy). In the context of a complete thermo-elastic study (not only thermal study), these types of measuring techniques guided us to set up a visible-range transparent vacuum chamber wall with an infrared-range transparent window, in such a way that any device under test (DUT) inside the chamber could be scanned by a variety of cameras. Another example of photogrammetry inside a vacuum chamber can be found in Ref. [24]. An example of using interferometry to measure the deformations of a breadboard telescope throughout thermal vacuum experiments is given in Ref. [25], demonstrating a dimensional stability corresponding to an overall Coefficient of Thermal Expansion (CTE) lower than 10^{-7} K^{-1} over a temperature range that exceeds 100 °C. The use of Carbon Fiber Reinforced Polymers (CFRP) allows to maintain small deformation in large structures. One hypothesis could be that the performance of the HSI is not critically influenced by the thermal loads, because its structure is comparably smaller than previous examples. A smaller size implies smaller displacements in terms of length variation. Therefore, larger sizes could result in increased instability and smaller ability to hold precise alignment. However, the material of the HYPSON HSI-platform is aluminum, whose CTE is much bigger than for CFRP, and consequently, the length variations for the same temperature changes. In Ref. [26], they carried out experimental correlation of a thermal model of a spacecraft structure for the thermoelastic analysis, by means of an infra-red camera and thermocouple sensors. They use a specific thermoelastic test demonstrator, covering the non-black outer surfaces with black tape to be better captured by the camera. They used heater lines to configure

different thermal gradients on the test item. Their thermal model could be well correlated with thermocouple sensors at given points, but it demonstrated not to be accurate enough to simulate large thermal gradients observed by the infrared camera. The thermal mesh in ESATAN was refined to improve the correlation. They also made a quantification of errors, categorizing them in (a) camera and temperature measurement inaccuracies, and (b) post-processing of infrared images and spatial mapping of the thermal model.

To validate the thermal model and to characterize the HSI thermal performance, testing activities are critically important. Different optical parameters are influenced by the temporal temperature change, each requiring a different experimental setup. Therefore, it is important to choose the optical parameters that are our experiment target. For the HYPISO-project, the FWHM is a relevant parameter, as we want to focus on the spectral resolution to be able to detect and distinguish different algae species in ocean waters [9]. In addition, Ref. [27] studied the spectral response in thermal environments, where the focus was on the FWHM of a reference peak in the spectral HSI response, and the intensity. Therefore, we will focus on the same parameters in this study, as the same type of HSI is studied. Another parameter that is used to compare optics properties is the Point Spread Function (PSF), which is often used for as a measure for the spatial performance of an imaging system. In Ref. [28], a method is developed for measuring the PSF for characterization of co-registration and resolution of hyperspectral cameras. However, the difference between our tests on the hyperspectral camera and for example the study of Ref. [28] is that the HSI is tested inside a vacuum chamber and subjected to thermal loads. Making the experimental set-up used in Ref. [28] and making it work with the vacuum chamber are out of scope for this project, as we focus on the in-house-made Thermal-Vacuum (TVAC) chamber set-up allowing for functional testing in space environment of optical payloads, within a low-cost space project.

This research is also included in a broader study of thermoelastic effects in optical space instruments. In the broader study, the thermal, structural and optical models are chained to get the relationship between temperature maps and FWHM and throughput parameters. Therefore, verification of the optical and thermal model by experimental tests is needed, and its results are shown in this paper.

In this paper, we describe the experimental set-up of a vacuum chamber with heater pads inside to adjust the temperature of the DUT, to test the HSI designed for the HYPISO CubeSats. We use the thermal results to verify the thermal model of the HSI, which can be used later for the in-orbit thermal control and for the thermoelastic analysis. In Ref. [27], the experimental equipment used was based on a thermal chamber with atmospheric pressure. Besides, a detailed thermal model of the HSI was not available at the

time. The description of the design of the HSI used in these tests can be found in Refs. [29, 30]. As a summary, relative displacements due to thermal gradients between optical parts will modify the FWHM and throughput parameters, and here, the tests to measure these relationship between the thermal loads and the optical outputs are presented. The paper is organized as follows: in Sect. 2, the experimental set-up is described. In Sect. 3, an HSI thermal model inside the vacuum chamber is presented and the model correlation is described in Sect. 4. In Sects. 5, 6, and 7, the results, a discussion on results, and the conclusions are outlined, respectively.

2 Experimental set-up

An in-house TVAC has been made at NTNU. The TVAC has an inner pressure lower than $3 \cdot 10^{-4}$ mbar, which is enough vacuum level to test the hyperspectral camera out of air conditions. A restricted thermal control capability is available to heat the DUT, from room temperature upwards. The chamber has one electrical feedthrough for heater pads, and a cross-feedthrough for the HSI Ethernet cable, the temperature sensors, the HSI power supply, and a high vacuum pressure sensor (see Table 1 and Fig. 1). The pressure sensor, temperature sensors, and heating pads inside the chamber are controlled by the Fancy Thermal Test Rig version 4 (FTTRv4), which is developed at NTNU. The FTTRv4 reads the sensor outputs, and provides an interface to adjust the heating pad temperatures. Besides, the chamber has a visible-transparent access window in front of the front objective, and an infrared-transparent access window (an 8–12 μm AR Coated Germanium Window) located at the chamber top plate. For thermal control of DUTs inside the vacuum chambers, there are (a) an infrared camera of a spectral range between 8 and 14 μm ; (b) 5 temperature sensors for point measurements; and (c) heater pads for heating the DUT platform. It can be observed that the range of wavelength of the window glass is narrower than the range of measurements of the infrared camera. The presence of radiative reflections between surfaces inside the chamber, combined with the uncertainty introduced by the coated germanium window, creates a level of uncertainty in temperature measurements. However, this can be addressed by incorporating contact sensor measures. By comparing the readings from both contact sensors and IR camera, the differences in temperature can be determined across the entire measured range. As the contact sensors only provide points of information, and the IR camera covers the entire area, the IR camera remains a valuable tool for characterizing thermal gradients. The complete list of elements that compound the test system is presented in the Table 1. The HSI is focused on an argon spectral lamp that is located outside the vacuum chamber.

Table 1 Breakdown of test system

System elements	Parts of the system elements	Description
Vacuum chamber	Baseplate	Aluminum plate to support DUTs and two accessing circular points
	Dome	Cylindrical glass with an external metallic grid protection
	Top plate	Aluminum disk plate with two access available
	Backing pump	Pumping down from 1 atm to around 0.3 mBar
	Turbo pump	Pumping down from 0.3 mbar to around 2E-4 mBar
	Infrared window	A 50 mm-diameter glass that is transparent within the range between 8 and 12 μm
	Visible window	A rectangular hole is made in the grid protection to provide certain field of view to HIS
	Cross feedthrough	Four sealing accesses in a cross to: (1) vacuum chamber, (2) Ethernet connector, (3) high vacuum pressure sensor, and (4) 7-pin electrical connector
	Electrical feedthrough	6-pin electrical connector where two of them are for heater pads supply
Thermal control system	Control system	Manual control for backing pump by valves, and digital control for turbo pump by display
	Temperature sensors	1-wire temperature contact sensors
	Heater pads	Rectangular electrical resistances: two of 1.25 W, two of 2.5 W, and two of 60 W
	Infrared camera	Camera in the spectral range of 8 and 14 μm for temperature mapping
	Power supply	Supply of current for heater pads with voltage control
Device under test	Sensor monitors	Monitoring of temperature contact sensors by FTTRv4 and temperature mapping by the IR camera software PIX connect
	HSI	Engineering model of the Hyperspectral imager for HYPISO
	CAN-USB	Communication system from field computer with Linux to DUT
	GSE Power supply	Ground segment power supply for DUT

The view of the HSI is cleared by making a small window in the protection cage around the vacuum chamber.

top plate of the vacuum chamber, where an access window made of infrared-transparent glass is available.

2.1 Thermal determination and control

The measuring system consists of temperature contact sensors and an infrared camera for temperature mapping from the top side. The thermal control system consists of heater pads attached to predefined locations and fed by a power supply. In Fig. 2, the heaters placed in the upper part of the platform are shown. In Table 2, the location and the purpose of the heater pads are presented. All heater pads are attached to the DUT platform because the objective is to increase the global temperature of the DUT, to obtain steady states in thermal balance tests. Once the control temperature is stabilized, the temperatures from the IR camera are used to correlate with the thermal model.

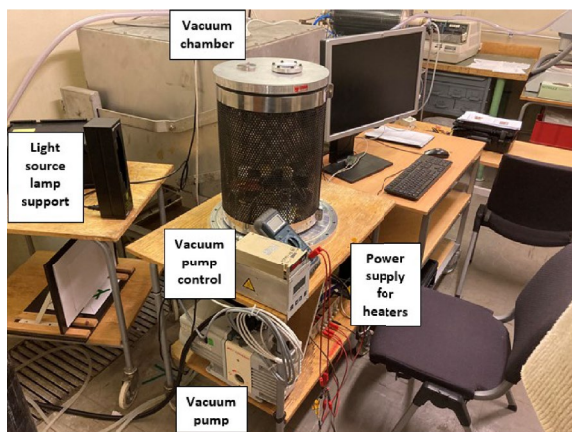
The infrared camera used is the Optris PI 450i-Optics O53, and the main characteristics are shown in Table 3. The infrared camera is used to monitor the temperature gradients of the HSI, as one of the targets of the test campaign is to verify the HSI thermal model that will be included in the whole thermo-elastic study. To have a useful temperature map, the infrared camera shall point perpendicular to get the more representative view of the camera. In our case, the top view allows monitoring all the HSI components, so that the camera is placed at the

2.2 Device under test

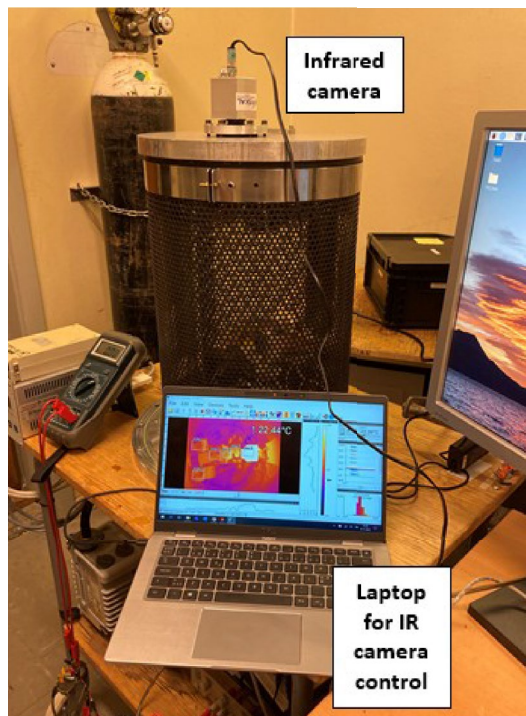
The DUT is the HYPISO-1 engineering model of the HSI joined to its platform. A schematic ray trace of the HSI can be seen in the top left of Fig. 3. The design of the HSI is optimized for imaging objects infinitely far away, as the HSI is used on a small satellite. Therefore, the light rays are assumed to enter the front lens (L0) as a collimated beam, and they are focused by L0 after which the entrance slit (S) is reached. The collimator (L1) forms a parallel beam that reaches the 300 grooves/mm transmission grating (G). The transmission grating disperses the rays. Lastly, the light rays are focused by (L2) to the sensor. Due to the wave properties of light, constructive and destructive interference can occur when two wave sources with different initial phase difference or path difference act together. The main equation describing this is called the grating equation

$$n\lambda = a(\sin\alpha + \sin\beta), \quad (1)$$

where n is the spectral order, λ is the wavelength, a is the groove spacing for a 300 grooves/mm grating, α is the incident angle and β is the diffracted angle, see Fig. 3. For collimated light beams, $\alpha = 0$.



(a) Vacuum chamber



(b) Infrared camera

Fig. 1 Elements of the thermal vacuum test system

The HSI has been placed in the Vacuum (VAC) chamber as shown in Figs. 2 and 4. The three objectives are made from aluminum 6061. All in-house machined parts of the HSI, including the slit tube, grating holder, sensor housing, and the payload platform with brackets to keep the components in place, are made from aluminum 6082. The platform is supported by four rods, threaded in the holes through the dampers holes. An additional frame is positioned in the bottom part of the rods to geometrically stabilize the assembly and avoiding the tilting of the four rods. In the HYPISO-1 engineering and flight models, the HSI and Red–Green–Blue (RGB) camera platform is joined to the CubeSat structure

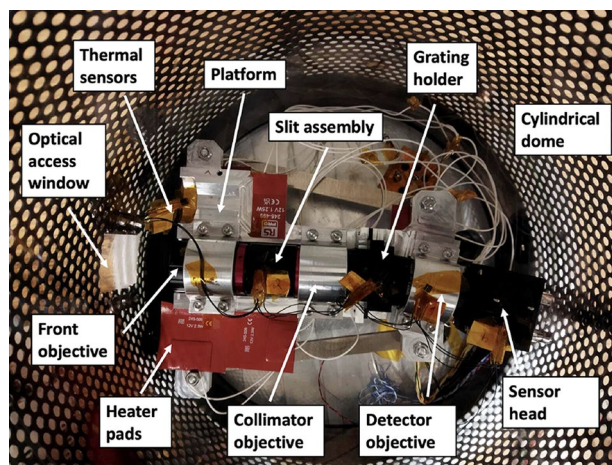


Fig. 2 Preliminary set-up of the HSI inside the vacuum chamber, with temperature sensors and heater pads for thermal control. An optical access window is available

Table 2 Location of heater pads in test configuration for temperature leveling purpose

Heater pad ID	Maximum heating power	Location
HT60A	60 W	Under HSI platform
HT60B	60 W	Under HSI platform
HT2.5A	2.5 W	Over HSI platform
HT2.5B	2.5 W	Over HSI platform
HT1.25A	1.25 W	Over HSI platform
HT1.25B	1.25 W	Over HSI platform

Table 3 Characteristics of the infrared camera

Characteristic	Values
Temperature range	– 20–100 °C
Spectral range	8–12 μm
Detector	382 × 288 pixels
Frame rate	80 Hz
Distance between the infrared and HSI	0.4 m
Pixel size at 0.4 m	0.4 mm
Recommended smallest measured object size	3 × 3 pixels
Smallest measured object at 0.5 m	1.38 × 1.38 mm
Focal length	8 mm
Angle of 53°: HFOV at 0.5 m	0.5 m
Angle of 38°: VFOV at 0.5 m	0.35 m
Angle of 66°: DFOV at 0.5 m	0.61 m
Angle of 2.2 mrad at 0.5 m: IFOV	1.1 mm
System accuracy	± 2 °C
Temp. sensitivity at 40 Hz and 25 °C room temp	40 mK
Emissivity	0.1–1.0

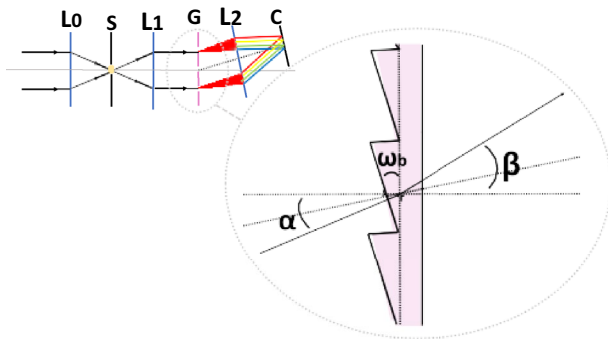


Fig. 3 A schematic ray trace of the HSI zoomed in on the blazed diffraction grating, which is the critical component of the HSI dispersing the light

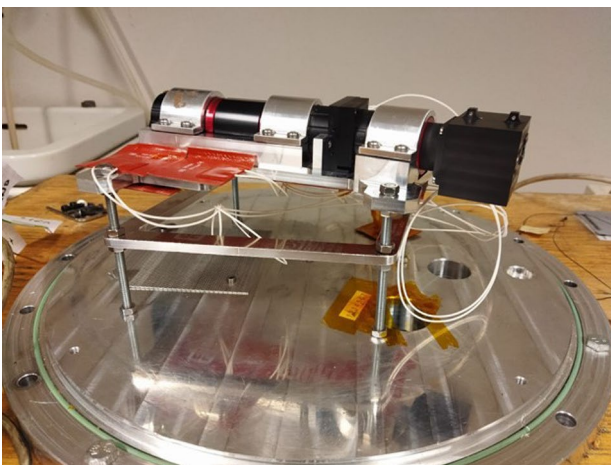


Fig. 4 Lateral view of the DUT

through four dampers for structural isolation and thermal insulation of the payload. The interface solution in flight was designed to meet the space limitations in the front of the bus. Each interface consists on a damper pair (model 21514S provided by SMAC) joined by a single M6.5×35 mm bolt to an aluminum 6082 T6 part with notches to accommodate the geometry of the bus frame. Finally, the aluminum part is attached to the frame bus with four M2.5 countersunk screws. The DUT is placed inside the chamber in such a way there is no contact with the cylindrical dome, and a free thermal deformation is allowed in any direction.

2.3 Typical in flight temperatures

The HYPISO-1 HSI in orbit measures the temperature during image acquisition. The temperature in the HSI sensor is typically 10–20 °C when no images are acquired. During nominal image acquisition, the sensor is turned on for approximately 43 s, and the temperature increases

about 5 °C. Three examples of temperature increase for longer image acquisitions are shown in Table 4. From these experiments, it can be seen that the temperature increases significantly with longer acquisitions, reaching close to 40 °C in the sensor. The other temperature sensors in flight are attached to the batteries and the electronic power system, and they measured average temperature values of 11.7 ± 0.9 and 8.1 ± 1.6 °C, respectively, over a period of 11 months. The minimum and maximum values for the batteries are 8.0 and 14.7 °C in this period, and for electronic power system 2.3 and 13.5 °C. This shows that the temperature inside the satellite is normally around 10 °C. In this work, we want to use the heater pads to reach temperatures of the HSI in the range for normal image acquisition (around 20 °C), increased image acquisition times (30 °C), and for successive increased image acquisition times (50 °C).

2.4 Test procedure

To compare results between the three cases tested (ambient and heaters ON with 8W and 32W of power dissipation), a systematic procedure was followed to set-up each test system component in all of them. In this manner, the uncertainty sources during the tests were equivalent, and their influence on the comparative results neglected. A summary of the step-by-step test procedure is presented in Table 5. After the cleaning of all surfaces that are immersed in vacuum environment during the tests, the chamber base plate is configured with the HSI, the heaters, and the temperature contact sensors. Then, the chamber is closed by placing the cylindrical transparent glass and the top plate. The infrared camera is set on the top plate window for mapping temperatures, and the light source lamp in front of the HSI, front objective for being the target of the image acquisitions. The measuring system and the vacuum pumps are switched on. Once the appropriate pressure levels are reached inside the TVAC, the heaters are switched on to obtain the desired temperature level in the DUT platform, and the HSI is turned on without acquiring images, to achieve a stationary thermal state. Then, hyperspectral images can be acquired with the HSI.

Table 4 Temperature increase in the HSI sensor with longer image acquisitions with the HYPISO-1 CubeSat in orbit

No	Date	Duration	FPS	Frames	Temperature
1	25 Aug 2022	1 min 27 s	11	956	20.6 to 31 °C
2	25 Aug 2022	2 min 39 s	6	956	22.3 to 38.3 °C
3	1 Dec 2022	3 min 14 s	5	956	18.4 to 39.8 °C

Table 5 Summary to step-by-step test procedure

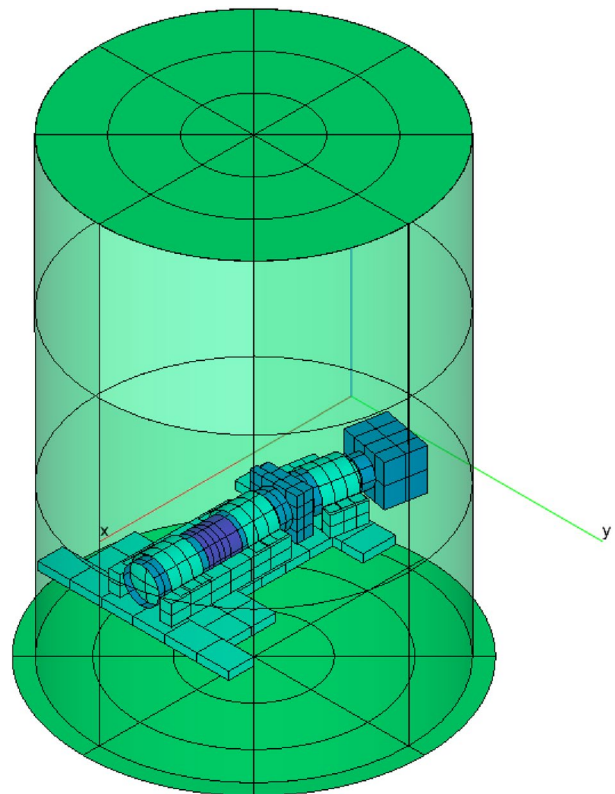
Procedure step	Description
Cleaning	Clean the inside of the cylindrical dome glass with a fiberless wipe and soap. Then, the glass, the top and bottom plates, the inner cables, and the DUT were cleaned with wipe and ethanol
Chamber setup	Place the DUT on the bottom baseplate; attach the temperature contact sensors on defined positions; connect the Ethernet and power cables to HSI; place the cylindrical glass taking care of not damaging the cables; to close the chamber with the top plate
Vacuum setup	Turn on the water for cooling; start the backing pump up manually to reach 0.3 mbar; and start the turbo pump by the display up to reach 10^{-4} mbar
Reference measuring	Take temperature measurements with the contact sensors and the IR camera; and take pictures with HIS
Thermal case setup	Switch on the power supply for heaters by setting a defined voltage; and wait until it reaches steady state conditions
Turn on spectral lamp	Turn on the argon spectral lamp that is already in focus of the HIS
Measuring	Take temperature measures with the contact sensors and the IR camera; take pictures with HIS
Post-processing	Import HSI data from uEye software, from the IR camera software, and from the temperature contact sensors; convert the picture made by the HSI detector in intensity-wavelength charts; and calculate the FWHM for each distinctive argon peak

3 Thermal model of the tests

In parallel to the experimental set-up, a thermal model of the hyperspectral camera within the thermal vacuum chamber is implemented with ESATAN-TMS. The purpose of this thermal model is to be inserted in a global analysis chain of a thermoelastic study on the HSI performance in-orbit. However, first, it is needed to verify the results of the thermal model with these experiments. The model is divided in the Geometrical Mathematical Model (GMM) and the Thermal Mathematical Model (TMM), which are described in the following two subsections, after the exposition of the thermal requirements. In Fig. 5, the GMM of the HSI within the thermal vacuum chamber is shown. In Fig. 6, a comparison of the HSI GMM obtained with the ESATAN-TMS (a) and the CATIA (b) is also shown.

3.1 Thermal requirements

From the HYPSON-1 that is currently in orbit, it is known that the HSI on board of HYPSON-1 is immersed in an environment with temperatures ranging between 10 and 30 °C. During image acquisitions, it was seen that the temperature of the sensor head increases. This is the main reason to set up a heating system in the vacuum chamber to characterize the HSI in increasing temperatures. Then, the thermal requirements are given in terms of the temperatures of the sensor head. They are 60 °C and 50 °C for upper non-operative and operative limits, respectively. These requirements will be considered all along the simulations and in experimental campaigns to ensure the thermal integrity of the camera. The thermal design of HSI is based on passive elements that allow appropriate equilibrium temperatures

**Fig. 5** Thermal model for thermal vacuum tests

for all thermal cases that are expected in orbit. The passive elements identified in the HSI are the thermo-optical properties of machined aluminum and the dampers, which allows to isolate from radiative standpoint and conductively the instrument by the cubesat platform.

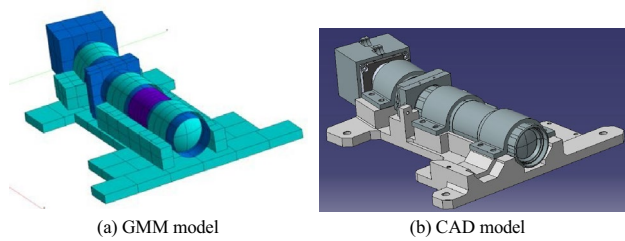


Fig. 6 Comparison of the geometrical mathematical model (made in ESATAN) and CAD model (made in CATIA)

Table 6 Values of thermo-optical properties ([31] and [32])

Therm-optical property	Infra-red emissivity	Infra-red transmittivity
Optical glass	0.07	0.93
G116 reverse A	0.89	0.0
G116 obverse	0.86	0.0
Anodized black	0.89	0.0
Bare Aluminum	0.035	0.0
Glass B270	0.081	0.919
N-F2 coat	0.003	0.997
N-LAK14 coat	0.002	0.998
N-SF57 coat	0.009	0.991
N-LASF44 coat	0.002	0.998

3.2 Geometrical mathematical model (GMM)

The GMM is based on the geometrical information of HSI internal and external components given in the Computer-Aided Design (CAD) model. Figure 6 shows an external view of the HSI CAD model and of the ESATAN GMM. It is remarked that the GMM is aimed to represent relevant surfaces for the radiative exchange calculation, so that only the ones with a big area have been included. The different elements of the HSI GMM are grouped into 6 hierarchical items: Front Objective (FOB), Slit Assembly (SLA), Collimator Objective (COB), Grating Assembly (GRA), Detector Objective (DOB), and Detector Box (DET). To use the thermal model for the vacuum chamber tests, the HSI platform and the vacuum chamber are also geometrically modeled (see Fig. 5). The reference system has the axis x aligned with the front and collimator objectives as well as the slit assembly, the vertical axis z is perpendicular to the HSI platform, and the axis y to complete a right trihedral system.

The heat exchange by radiation between the GMM surfaces depends on the mutual field of view and on their thermo-optical properties. The values of infrared emissivity and solar absorbance are presented in Table 6, and their locations in the model are shown in Fig. 7. The values of

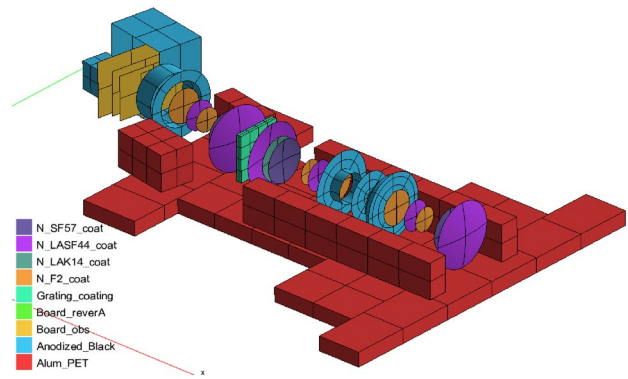


Fig. 7 Thermo-optical properties of the HSI elements ([31] and [32])

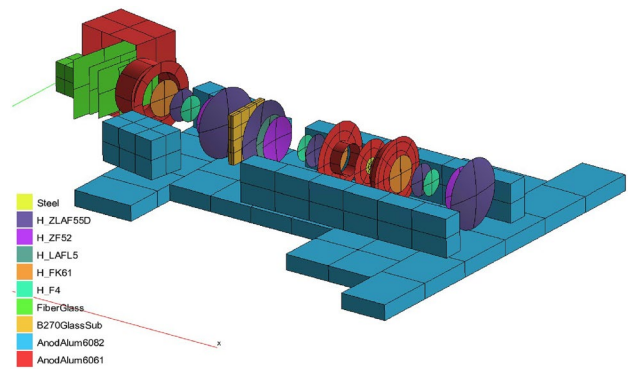


Fig. 8 Distribution of the bulk properties along the HSI components ([31] and [32])

thermo-optical properties of opaque materials were considered from Ref. [31], while the values of lenses are extracted from Schott optical glass collection datasheets [32]. Regarding the diffuse reflectivity, we have considered that is one minus the emissivity for opaque materials and negligible for transparent lenses.

3.3 Thermal mathematical model (TMM)

The TMM includes the definition of the bulk materials, the conductive couplings between nodes, the power dissipation of components, the definition of the analysis cases, and the calculation of the temperatures and heat fluxes for each thermal case. The bulk materials used are shown in Fig. 8, and the values of thermal properties are presented in Table 7.

As usually done in space systems, the thermal model should be verified. Environmental tests or sensitivity analyses are used to gain confidence on the thermal model. The verification is needed to reduce the inherent uncertainty in many of the thermal parameters used or calculated during the modelization process. The Linear Conductors (GLs) between shells is one of the main uncertainty sources

Table 7 Values of bulk properties ([31] and [32])

Bulk property	Density [kg/m ³]	Specific heat [J/(kg K)]	Thermal conductivity [W/(m K)]
Fiber Glass	2540	787	1.1
Steel	4600	525	22.15
aluminum 6061	2770	896	167
aluminum 6082	2770	896	170
Glass B270	2550	800	1
Optical glass	2560	800	1
H-LAFL5	3630	630	0.89
H-ZF52	3530	660	0.99
H-F4	2650	810	1.05
H-ZLAF55D	4440	530	0.82
H-FK61	2650	810	1.05

in a thermal model. The ones with a common edge are calculated by ESATAN-TMS, but the rest of connections without a physical representation in the GMM must be computed manually (more than 250 linear conductors in our model).

A description of the different types of calculated linear conductors is as follows: To define the conductive interface of different model subparts belonging to the same machined part, a fused GL is defined, so only conductive resistance across the materials is considered. An example of this type of linear conductor is found between the HSI platform and the upwards extensions for the bracket joints. The shell thickness, the model node width, and the distance from the center of the node to the contact line center are needed. Other structural connections have a contact resistance (i.e., brackets to platform extensions), because they are bolted to each other. In these cases, a contact conductance was added to the conductive resistance through the materials. Depending on the bolt diameter, the washers, and the applied torque, the value of the contact conductance can vary. A contact conductance of 500 W/m² K is used for tight contact areas, like the brackets to the objective cylindrical surfaces [31]. The contact conductance through the screw teeth is modeled as 300 W/m² K, like the joints between both sides of the grating housing. These values are based in the experiments of other authors given in Ref. [31].

Linear conductors must be defined to quantify the heat transferred through electrical pinned connectors: (1) the power supply and (2) the Ethernet cable. A linear conductor is defined for each pin, so the total conductance of the connector is computed multiplying by the number of pins. The linear conductor of one pin is computed with two conductive resistance (male and female parts) and a contact conductance of 500 W/m² K, because the pin must be tightly connected to ensure electrical conductivity. The list

of conductive couplings with linear conductors that has been correlated is shown in Table 10.

The internal heat exchange is provided by external and internal heat sources. With the spacecraft in orbit, the solar, albedo, and planet fluxes are considered as external sources, and power consumption of electronics components as internal ones. However, the HSI thermal model is used here to be inserted in a complete thermoelastic analysis chain that is verified with experiments in a thermal vacuum chamber. Therefore, the HSI external environment is considered to be the chamber glass dome and the bottom base plate, which maintain room temperature all along the tests (see Fig. 5). As the HYPSONO payload is inside the CubeSat platform provided by NanoAvionics, whose thermal control subsystem provides a stable thermal enclosure, the external environment during tests would be not far from the one in orbit. Within the nominal range of inner temperatures in HYPSONO, the main variation is an increase when HSI is operating. Therefore, as explained in Sect. 2.1, a heating system with a total of 127.5 W is available inside the vacuum chamber, which was used for increase the temperature of the HSI platform in the reference thermal balance case. In the thermal model, power dissipation due to electronics components working is modeled as nodes producing inner heating power, which takes place at the detector box. In our laboratory tests and in the thermal model, only the detector box is dissipating power, and this is distributed in the four boards inside the detector box. For all the steady cases studied (heaters at different power levels), the camera is always switched ON.

4 Thermal model in-house correlation

Methodology A method for fitting the thermal models inside vacuum chambers with only heating capability is proposed. This type of methodology can be very useful for low-cost space projects, where only facilities with limited capabilities are accessible. The main steps are:

- The thermo-optical properties of the surfaces and the bulk properties of the materials are previously obtained from bibliography.
- The values of the linear conductors (GLs) between nodes in the thermal model are preliminary adjusted with the ambient temperature case with no heating power.
- A given power is set in the heater pads power supply. The values of the heating power are set in the thermal model corresponding with the nominal amount of power applied in each analysis case (see Table 8). However, due to, in between other factors, the uncertainty in the effective heat transfer from the heater to the aluminum platform, their dissipation power is considered as a fitting parameter in the correlation process. Moreover, there are

Table 8 Applied heater values for each heater pad (presented in Table 2) and for each analysis case (AC)

Heater pad ID	AC-Amb [W]	AC-8 [W]	AC-16 [W]
HT60A	0	3.8	15
HT60B	0	3.8	15
HT2.5A	0	0.2	0.6
HT2.5B	0	0.2	0.6
HT1.25A	0	0.1	0.3
HT1.25B	0	0.1	0.3

other dissipation sources as the current within the cables, so that they have been considered in the thermal model by applying a power equal to the heat dissipated by Joule effect directly in the same positions as the heaters.

- The thermal model can be run at other thermal cases different than the cases used for the correlation, by keeping the fitted GLs and by scaling the power dissipation values.

5 Results

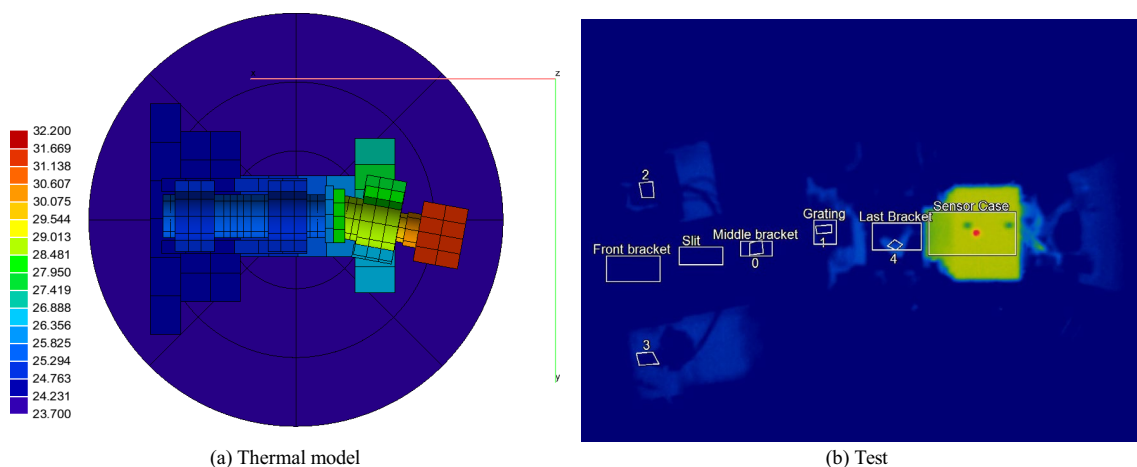
The main objectives of the test campaign were to characterize the HSI in vacuum and thermal environment, and to verify its thermal model. Therefore, the test cases (presented in Table 8) were planned to have several temperature levels in the HSI platform. Thus, several images were taken with the HSI at each temperature level. The higher the power applied to the heater pads, the higher the thermal gradients are along the HSI components. As mentioned above, the verification process consists of: (a) recreating the same thermal scenario with ESATAN in terms of boundary temperature, heat dissipation on the heaters, and HSI sensor head; (b) modifying

the linear conductors of the thermal model with the ambient case; (c) modifying the heat dissipation values; and (d) obtaining similar temperatures as measured ones at target positions (the correlation criteria used is ± 5 °C).

The heater pad configuration is presented in Table 2. Tests with and without vacuum were performed to compare the HSI images. The measured temperatures were maintained within a rate of temperature change of 1.0 °C during 1 h. Just later, the HSI was used to take frames for about 25 s, taking 10 captures in each configuration. Temperatures in the platform were around 23 °C for 0 W-heaters, 33 °C for 8W-heaters and 50 °C for 30 W-heaters. First and last temperatures were used to do the thermal model correlation, and the middle one to check it.

5.1 Temperature results

The measures of temperatures with the IR camera are compared with the temperatures obtained with the thermal model. A snapshot of the measurements of the IR camera for each temperature objective can be seen in Figs. 9b, 10b, and 11b, where the temperature sensors are shown by the contours 0 to 4. The temperatures measured with the IR camera have been verified by comparing the temperatures of the contact sensors with the infrared camera measures of areas in the same location as the contact sensors (see Table 9). Most of temperatures measured by the contact sensors and the IR camera seem to be reasonably similar, except the IR camera measure in the area of the contact sensor 2. This is in the platform close to one of the 1.25 W heater pads, and the extremely hot temperature could be a consequence of the reflection of the IR radiation emitted from the heater or the surrounding cables. A hotter temperature in Figure 10b and 11b in the +x side of the sensor head can be seen. The material on the +x side is aluminum 6060, and the remainder of

**Fig. 9** Temperature map of HSI for the thermal model and for the tests during the room temperature case. No power applied in the platform

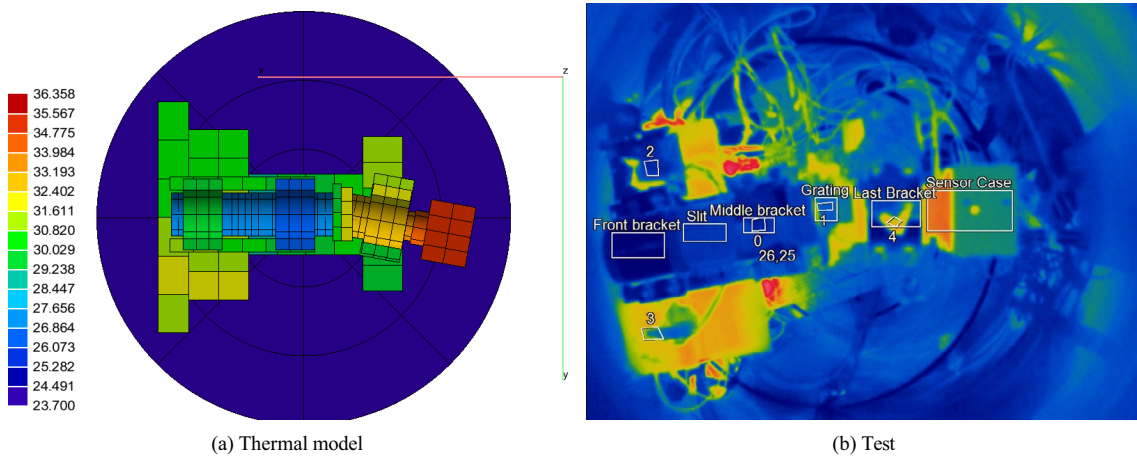


Fig. 10 Temperature map of HSI for the thermal model and for the tests during the hot case. A total power of 8 W applied in the platform

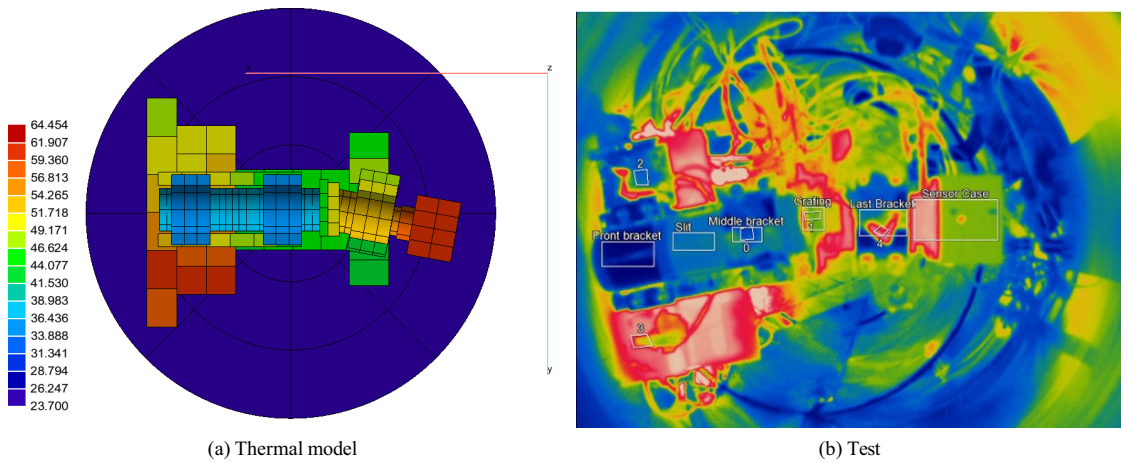


Fig. 11 Temperature map of HSI for the thermal model and for the tests during the hot case. A total power of 32 W applied in the platform

Table 9 Temperature comparison between IR camera ($T_{IRcamera}[C]$) and contact sensors CS ($T_{contactsensor}[C]$).

Sensor location	$T_{CS,0W}$ [C]	$T_{IRcam,0W}$ [C]	$T_{CS,8W}$ [C]	$T_{IRcam,8W}$ [C]
BRA COB (CS0)	22.9	22.9	25.2	25.1
GRA (CS1)	23.7	24.0	27.4	27.5
PLT -Y (CS2)	23.1	22.8	26.4	36.9
PLT +Y (CS3)	23.6	24.8	28.2	25.9
BRA DOB (CS4)	23.8	26.1	27.2	29.0

Ambient case: Heater power of 0 W. Hot case: Heater power of 8 W

the sensor case is made of aluminum 6082. There are no heater pads used to increase the temperature of the sensor case. One possible reason for this effect is reflection of the surrounding power cables to the HSI sensor. In addition,

this part of the sensor is not perpendicular to the IR camera, whereas the remainder of the sensor case is perpendicular. To represent the different IR camera view angles as good as possible, we decided to take an average area of both surfaces to estimate the temperature.

Each thermal node in the ESATAN model is assigned to a specific area, resulting in the calculation of a temperature value for the center of the node. In the thermal model, we have used average values for a group of nodes, which correspond to the areas that have been also averaged in the IR camera software. Before and after fitting the linear conductors in the thermal model, the preliminary and corrected temperatures are shown in Table 10. As mentioned above, the linear conductors manually implemented in ESATAN contain an inherent uncertainty due to the use of reference values for the material thermal conductivity k , the contact conductance in the node interface h_c , or the approximation

Table 10 Temperature comparison between measured

HSI component	$T_{\text{measured}-0\text{W}}$ [°C]	$T_{\text{calc}-0\text{W}}$ [°C]	$\delta T_{0\text{W}}$ [°C]
SLIT	23.1	25.3	2.2
GRA (CS1)	23.9	26.0	2.1
DET	35.3	31.4	- 3.9
PLT (CS2)	23.0	24.4	1.4
PLT (CS3)	24.2	24.3	0.1
BRA FOB	22.9	25.1	2.2
BRA COB (CS0)	22.9	25.1	2.2
BRA DOB (CS4)	25.0	28.9	3.9
Temperature mean deviation of $\delta T_{0\text{W}} = 1.3$ °C Temperature standard deviation of $\delta T_{0\text{W}} = 2.3$ °C			
HSI component	$T_{\text{measured}-8\text{W}}$ [°C]	$T_{\text{calc}-8\text{W}}$ [°C]	$\delta T_{8\text{W}}$ [°C]
SLIT	25.5	27.4	1.9
GRA (CS1)	27.5	30.1	2.6
DET	33.6	35.5	1.9
PLT (CS2)	31.7	30.6	- 1.1
PLT (CS3)	27.1	31.9	4.8
BRA FOB	33.6	29.6	- 4.0
BRA COB (CS0)	25.2	26.8	1.6
BRA DOB (CS4)	28.1	32.9	4.8
Temperature mean deviation of $\delta T_{8\text{W}} = 1.6$ °C Temperature standard deviation of $\delta T_{8\text{W}} = 2.9$ °C			
HSI component	$T_{\text{measured}-32\text{W}}$ [°C]	$T_{\text{calc}-32\text{W}}$ [°C]	$\delta T_{32\text{W}}$ [°C]
SLIT	32.9	35.9	3.0
GRA (CS1)	45.2	45.5	0.3
DET	60.7	61.9	1.2
PLT (CS2)	47.1	51.4	4.3
PLT (CS3)	62.8	61.6	- 1.1
BRA FOB	29.8	34.8	5.0
BRA COB (CS0)	33.6	34.7	1.1
BRA DOB (CS4)	57.8	53.6	- 4.2
Temperature mean deviation of $\delta T_{32\text{W}} = 1.2$ °C Temperature standard deviation of $\delta T_{32\text{W}} = 3.0$ °C			
Fitting of linear conductors			
Node A	Node B	GL before fitting [W/K]	GL after fitting [W/K]
FOB BRA	FOB	0.4712	0.0001
COB	BRA COB	0.4712	0.0001
COB	GRA Front	0.0011	0.0080
GRA Front	GRA Back	0.0031	0.0031
GRA Back	DOB	0.5498	2.0000
DOB	BRA DOB	0.4712	6.0000
DOB	DET	0.1508	2.4000
BRA FOB	PLT	0.2783	0.0001
BRA COB	PLT	0.2783	0.0001
BRA DOB	PLT	0.2783	8.0000
GRA	PLT	0.3711	16.0000
DET inside	DET	15.1098	33.2000

Temperatures (T_{measured}) and thermal model ($T_{\text{calculated}}$) temperatures. Values of linear conductors (joining nodes A and B) before and after the model fitting. Ambient case: 0 W. Intermediate case: 8 W. Hot case: 32 W. Average temperature of contact sensors and IR camera measures. Correlation temperature difference of 5 °C

of the physical geometry to simple shape volumes (cross-sectional area of the heat path, A , and distance between node centers l). Between two separated thermal nodes i and j , the GL is calculated as

$$GL_{ij} = \frac{1}{\frac{l_i}{k_i A_i} + \frac{1}{h_c A_j} + \frac{l_j}{k_j A_j}} \quad (2)$$

Most of linear conductors (all joining elements along the plane x - y , and in the vertical direction z if both joined elements are visible from top) can be adjusted with the temperature difference between prepared areas in the infrared camera. As the top view contains all the relevant parts of the HSI, it is enough to fit the thermal model.

The temperatures obtained with the fitted thermal model are presented together with the ones measured in the vacuum chamber in Figs. 9, 10, and 11. In the flight model (the HSI inside the CubeSat), the conductive couplings between the HSI and the rest of the structure is made by means of four dampers, which will insulate it thermally. This fact is considered in the tests separating the platform from the vacuum chamber base plate with four long rods that will reduce the linear conductors close to 0, see Eq. (2). However, this approximation of the HSI platform joints does not aim to represent the flight boundary conditions from the perspective of the thermo-elastic stress field, but rather to enable unobstructed deformation to obtain the largest possible displacements and thus evaluate the performance of the hyperspectral camera. In a similar manner, the radiative environment in the tests is not representative of flight conditions. The test campaign was to validate the thermal model for being inserted into a thermo-elastic models chain. The thermo-elastic model chain will give us the performance of HSI with different conductive and radiative boundary conditions, so the best design choices can be adopted for following versions of the HYPSONO CubeSat.

According to the European Cooperation for Space Standardization (ECSS) on thermal analysis [33], there are potential parameter variations that will produce uncertainties on the thermal simulation predictions of the tests. Some of the most relevant are: the chamber wall temperature of ± 10 °C; the temperature sensor measurement accuracy of ± 1.5 °C; or the nodal-sensor position error of ± 3 °C. On the other hand, there will also be a temperature difference between the temperatures measured during the tests and the temperature calculated by the thermal model. As stated in Ref. [34] for internal units, a maximum temperature difference of ± 5 °C is considered in our correlation process. Besides Ref. [34], also establishes two additional correlation success criteria for considering the thermal gradients between the different parts of the instrument and the data dispersion: (a) the temperature mean deviation within the range -2 to 2 °C; and (b) the temperature standard deviation lower than 3 °C

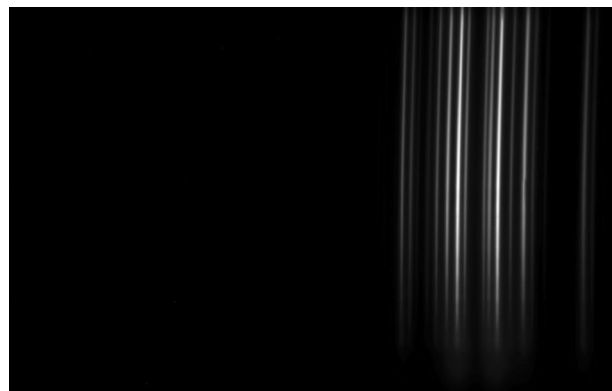


Fig. 12 Example picture taken by the HSI detector at room temperature (in vacuum) with the argon light source. The x -axis is wavelength (spectral axis), while the y -axis follows the slit length (spatial axis)

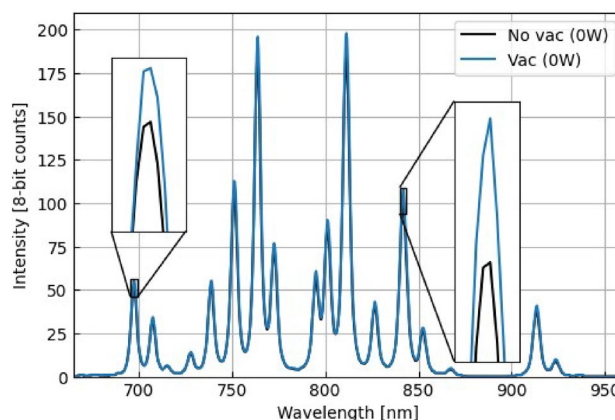


Fig. 13 Comparison of spectral response seen by the HSI of the argon lamp with and without vacuum at room temperature (0 W)

for 1 sigma. These parameters calculated in our correlation process are presented in Table 10.

5.2 HSI images

The optical performance of the HSI was characterized using the pictures taken during the tests. An example of a picture (spectrogram) taken at room temperature with the argon lamp is shown in Fig. 12. In order to characterize the HSI, the center position in the spatial axis (y -axis) of the image was used to avoid smile effects. The peaks in the spectral response (seen in Figs. 13 and 14) were then identified, and the full width at half-maximum (FWHM) for some of these peaks calculated by a Python script.

The spectral response was first compared before and after the vacuum chamber was turned on, to see the effects of vacuum, shown in Fig. 13. There is a slight change in the response, the peaks get higher, but no spectral shifts are visible.

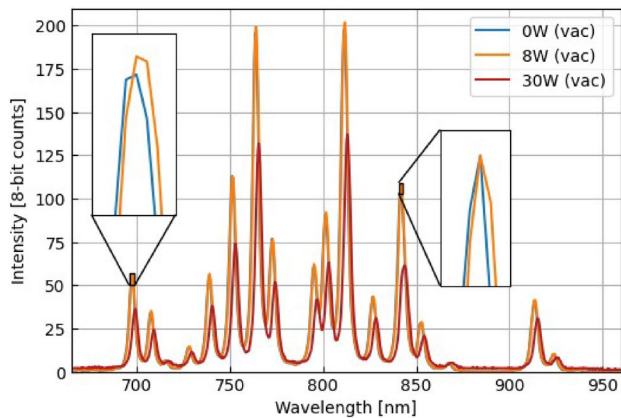


Fig. 14 Spectral response seen by the HSI of the argon lamp inside the vacuum chamber for changing temperatures

The spectral response in vacuum with changing temperature can be seen in Fig. 14. There is a small change in the response from 0 to 8 W, as seen in the zoomed in box plots, but less change in intensity than what was seen for vacuum/no vacuum. There does, however, seem to be a small spectral shift, moving the peaks from the warmer temperature (8 W) to the right, toward the longer wavelengths. For 30 W, however, a large spectral shift and change in intensity can be seen. This is due to the argon lamp being moved slightly between the 8 W and 30 W measurements. The spectral shift can possibly be explained by this movement. Since the HSI looks directly at the argon lamp, a small shift in lamp or HSI position will cause the light rays to enter at a slightly different position in the HSI front lens. Here, the field dependency gets noticeable as the light through the slit assembly might end up reaching the grating at a different angle. The angle α on the blazed transmission grating, as seen in Fig. 3, might therefore no longer be equal to 0, causing a difference in the angle of the dispersed light β , resulting in a spectral shift on the sensor.

The 30 W HSI measurement can therefore here not be used to verify the model. It shows, however, that the idea of the set-up works, but that the lamp either should be secured to ensure no movement, or that a stronger lamp illuminating a uniform diffuse surface should be used instead.

The FWHM values for the argon peaks can be seen in Fig. 15 (measurement at 30 W not included since the measurement is invalid due to movement in the set-up). Since this is a measure of the width of the peaks, it gives information about how the focusing of the light rays changes. It can be seen that the values are almost the same for all peaks. However, some deviations where the higher temperature (8 W) shows lower FWHM values can be seen. The average FWHM at room temperature (0 W) is 4.41 ± 0.55 nm, while the average FWHM for 8 W is 4.38 ± 0.54 nm, suggesting that the general trend is lower values for 8 W. This indicates

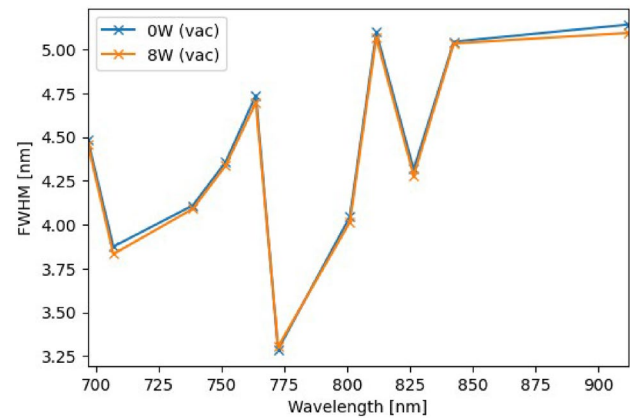


Fig. 15 Calculated FWHM for argon peaks in vacuum, at 0W (room temperature) and 8W

that the spectral focus has improved for these wavelengths with higher temperatures. This can further be used to compare with simulations and models of the optical response with changing temperature.

6 Discussion

In the experimental set-up, the goal was to perform image acquisitions in a vacuum chamber at three temperature levels matching in-orbit normal image acquisition (around 20 °C), increased image acquisition times (33 °C), and for successive increased image acquisition times (50 °C). As the current set-up had no cooling system, the first temperature is about 3 °C higher than we needed. One improvement to the set-up could be to install a cooling system inside the vacuum chamber to be able to cool parts. The higher temperatures were reached with the heating pad set-up.

In the verification process, given a correlation accuracy (in terms of temperature difference, temperature mean deviation, and temperature standard deviation), the thermal parameters with highest values of inaccuracy are first used to fit the temperature maps between the simulations and the tests. The linear conductors between HSI parts have been demonstrated to be appropriate for this task. As shown in Figs. 10 and 11, the temperature maps provided by the infrared camera include cables or electrical connections that in thermal model are not modeled. The heat radiation emitted by these hot cables may affect the temperatures of the surrounding parts, so they constitute another uncertainty source in the thermal model. To alleviate this uncertainty, the power dissipation through the heater cables has been modeled when the heaters are ON. The power dissipated in the cables is the voltage square divided by the cable resistance, which is equal to the electrical resistivity multiplied by the cable length and divided by the cross-sectional area of the cable.

In ESATAN, we have modeled this with a power assigned to the heater, which is proportional to the heat power dissipated all along the heater pad cable. As described in Sect. 4, once the linear conductors within the model have been fitted with the ambient thermal case, the virtual power of the heaters in the TMM increased with an amount proportional to the cable's length that is close to that heater pad, up to the model temperature which is within the predefined accuracy range of the test temperatures. Besides, the IR camera measures radiation reflections in some areas, such as the chamber plate in front of HSI, the top part of the brackets, or in the + x side of the sensor head. These factors complicate the process of model fitting. To solve this, the temperatures in the center of representative nodes of the thermal model are compared with the average temperature of the same component in the IR camera images. The temperature distribution along the camera shows a gradient from the detector to the front objective, but it becomes sharp in the interface between the grating and the collimator objective. This may be the consequence of the lack of a dedicated mechanical joint between both parts, combined with the fact the brackets applied pressure only in the z direction but not in the x direction. To prevent the reflection problems, the set-up with the IR camera should be improved. We should not only validate the temperatures we see with the temperature sensors, but we should also verify the temperatures in more detail for the reflecting components. One possible way could be to do extra tests with emissivity labels on the reflecting materials.

For the nominal temperatures that the HSI experiences on HYPSON-1 in orbit during normal operations (around 20 °C in HYPSON-1, 0W in experiments), and longer image acquisition (around 30 °C in HYPSON-1, and 8W in experiments), no difference in intensity, and only a small spectral shift is observed. The average FWHM decreases with a higher temperature. However, in the work of Ref. [27], the opposite relation was found; the FWHM increases with a temperature increase in TVAC controlled environment. In Ref. [27], it is discussed that additional temperature sensors are required to ensure temperature stability before taking measurements. In the new set-up in this work, multiple temperature sensors and an IR camera with live feed are used to ensure that the temperatures in are stabilized. One possible reason for the opposite relation found in our results is that it could be that temperatures of the HSI components in Ref. [27] were not stabilized yet. Another possible explanation for this inconsistency is in the optical properties of the HSI, as FWHM depends on whether the initial physical focal length of the HSI is smaller or larger than the optimal focal length. More experiments are needed to determine this shift in direct or inverse relation between FWHM and temperature. To determine this, a DUT with an initial physical focal length with a known deviation smaller than the optimal focal length should be set up. Then, images should

be acquired throughout the full spectrum that the HSI can capture (visible light to near IR) and the amount of measurements done should be made statistically relevant. This should be repeated *mutatis mutandis* for DUT with an initial physical focal length with a larger deviation than the optimal focal length. In addition, a (mathematical) optical model of the HSI could be set up to study the effect of displacement of each component of the HSI in more detail.

7 Conclusions

The development of thermal models for simulations and the use of vacuum thermal tests for the verification of those models are common practices in large space projects. Both tests and simulations are essential to comprehend the impact of design choices. However, in small satellites, low cost and short design periods limit the possibility to have realistic thermal models. Less common is the development of detailed thermal models of the CubeSat payload, and completely negligible the number of payload thermal models that were verified by tests in a vacuum chamber (separately from the CubeSat). In this paper, the detailed thermal model of the hyperspectral imager onboard the CubeSat HYPSON is presented, and its verification by comparing the temperature maps with thermal vacuum tests. The set-up of a transparent vacuum chamber with the heater pads that provide some thermal control in the DUT platform is presented. Besides, functional tests on the HSI were performed, in such a way, the chamber has been shown to be an appropriate test facility to characterize the thermal performance of the hyperspectral imager in a vacuum environment.

Author contributions All authors contributed to the study conception and design. Initial vacuum chamber set-up was made by [FSG], adaptation of the set-up and chamber accesses for the HSI tests was performed by [EO], [FN-M], and [AG]. Material preparation, data collection, and analysis were performed by [EO], [FN-M], [TAJ], and [MBH]. The first draft of the manuscript was written by [FN-M] and [EO], and all authors commented on previous versions of the manuscript. All authors read and approved the final manuscript.

Funding Open Access funding provided thanks to the CRUE-CSIC agreement with Springer Nature. This work was supported by the Research Council of Norway through the Centre of Excellence funding scheme (NTNU-AMOS, grant no. 223254) and the IKTPLUSS project MAS-SIVE (grant no. 270959), and the Norwegian Space Agency and the European Space Agency through PRODEX (no. 4000132515). Besides, the researcher Fermin Navarro Medina received a research grant by Spanish Ministry of Universities within the "Jose Castillejo" program of mobility stays abroad for young PhDs with reference number CAS21/00502, to stay in NTNU in Trondheim (Norway). Funding for open access charge: Universidade de Vigo/CISUG.

Data availability The data that support the findings of this study are mainly in the document, but if any additional information is requested, it could be provided by mailing the correspondence author.

Declarations

Conflict of interest All authors certify that they have no affiliations with or involvement in any organization or entity with any financial interest or non-financial interest in the subject matter or materials discussed in this manuscript.

Open Access This article is licensed under a Creative Commons Attribution 4.0 International License, which permits use, sharing, adaptation, distribution and reproduction in any medium or format, as long as you give appropriate credit to the original author(s) and the source, provide a link to the Creative Commons licence, and indicate if changes were made. The images or other third party material in this article are included in the article's Creative Commons licence, unless indicated otherwise in a credit line to the material. If material is not included in the article's Creative Commons licence and your intended use is not permitted by statutory regulation or exceeds the permitted use, you will need to obtain permission directly from the copyright holder. To view a copy of this licence, visit <http://creativecommons.org/licenses/by/4.0/>.

References

- Thornton, E.: Thermal Structures for Aerospace Applications, 1st edn. American Institute of Aeronautics and Astronautics, Washington DC (1996)
- Heesel, E., Weigel, T., Lochmatter, P., Rugi Grond, E.: Coupled thermo-elastic and optical performance analyses of a reflective baffle for the bepicolombo laser altimeter (bela) receiver. In: International conference on space optics— icso 2008 (2008). <https://doi.org/10.1117/12.2308252>
- Tse, L., Chang, Z., Slimko, E., Somawardhana, R.: Structural, thermal, and optical performance (stop) modeling and analysis for surface water and ocean topography mission. In: 48th International Conference on Environmental Systems (2018)
- Garcia-Perez, A., Alonso, G., Gomez-San-Juan, A., Pérez-Álvarez, J.: Thermoelastic evaluation of the payload module of the ariel mission. *Exp. Astron.* **53**, 831–846 (2022). <https://doi.org/10.1007/s10686-021-09704-0>
- Appel, S., Wijker, J.: Simulation of Thermoelastic Behaviour of Spacecraft Structures, 1st edn. Springer International Publishing, Cham (2021)
- Prentice, E.F., Grøtte, M.E., Sigernes, F., Johansen, T.A.: Design of a hyperspectral imager using COTS optics for small satellite applications. In: Proc. SPIE 11852, International Conference on Space Optics—ICSO 2020, pp.1185258 (2021)
- Henriksen, M.B., Prentice, E.F., Johansen, T.A., Sigernes, F.: Pre-launch calibration of the HYPPO-1 cubesat hyperspectral imager. In: IEEE Aerospace Conference (2022)
- Bakken, S., Henriksen, M.B., Birkeland, R., Langer, D.D., Oudijk, A.E., Berg, S., Pursley, Y., Garrett, J.L., Gran-Jansen, F., Honoré-Livermore, E., et al.: Hypso-1 cubesat: first images and in-orbit characterization. *Remote Sensing* **15**(3), 755 (2023)
- Grøtte, M.E., Birkeland, R., Honoré-Livermore, E., Bakken, S., Garrett, J.L., Prentice, E.F., Sigernes, F., Orlandic, M., Gravdahl, J.T., Johansen, T.A.: Ocean color hyperspectral remote sensing with high resolution and low latency—the hypso-1 cubesat mission. In: IEEE Transactions on Geoscience and Remote Sensing, vol. 60, pp. 1–19 (2022). <https://doi.org/10.1109/TGRS.2021.3080175>
- Dunwoody, R., Reilly, J., Murphy, D., Doyle, M., Thompson, J., Finneran, G., Salmon, L., O'Toole, C., Reddy Akarapu, S., Erkal, J., Mangan, J., Marshall, F., Somers, E., Walsh, S., de Faouite, D., Hibbett, M., Palma, D., Franchi, L., Ha, L., Hanlon, L., McKeown, D., O'Connor, W., Uliyanov, A., Wall, R., Shortt, B., McBreen, S.: Thermal vacuum test campaign of the eirsat-1 engineering qualification model. *Aerospace* (2022). <https://doi.org/10.3390/aerospace9020099>
- Stesina, F., Corpino, S., Borrás, E.B., Amo, J.G.D., Pavarin, D., Bellomo, N., Trezzolani, F.: Environmental test campaign of a 6u cubesat test platform equipped with an ambipolar plasma thruster (2022). DOI <https://doi.org/10.12989/aas.2022.9.3.195>
- Huang, B., Ma, Y.: Spacecraft Environment Test Technology. National Defense Industry Press, Taiwan (2002)
- Zhang, J., Lu, T., Ye, T., Li, F., Zhang, Y., Liu, X.: Development of an intelligent control system for spacecraft vacuum thermal test. *J. Phys.: Conf. Ser.* **1**, 2021 (1848)
- Müller, D., et al.: The solar orbiter mission. *Astronomy and Astrophysics* **642**, A1 (2020). <https://doi.org/10.1051/0004-6361/202038467>
- Garzón, A., Villanueva, Y.A.: Thermal analysis of satellite libertad 2: a guide to cubesat temperature prediction. *J. Aerosp. Technol. Manag.* (2018). <https://doi.org/10.5028/jatm.v10.1011>
- Richter, S.: Stop analysis for a spacecraft camera distortion model i. abstract
- Garzón, A., Tami, J.A., Campos-Julca, C.D., Acero-Niño, I.F.: Effect of beta angle and contact conductances on the temperature distribution of a 3u cubesat. *Thermal Science and Engineering Progress* **29**, 101183 (2022)
- Cubas, J., Gomez-San-Juan, A.M., Pindado, S.: On the thermoelectric modelling of smallsats. In: 2020 International Conference on Environmental Systems (2020)
- Pérez-Grande, I., Sanz-Andrés, A., Guerra, C., Alonso, G.: Analytical study of the thermal behaviour and stability of a small satellite. *Appl. Therm. Eng.* **29**(11–12), 2567–2573 (2009)
- Anvari, A., Farhani, F., Niaki, K.: Comparative study on space qualified paints used for thermal control of a small satellite (2009)
- Ali, A., Tong, J., Ali, H., Mughal, M.R., Reyneri, L.M.: A detailed thermal and effective induced residual spin rate analysis for leo small satellites. *IEEE Access* **8**, 146196–146207 (2020)
- Robinson, D., Simpson, R., Parian, J., Cozzani, A., Casarosa, G., Sablerolle, S., Ertel, H.: 3d thermography for improving temperature measurements in thermal vacuum testing. *CEAS Space Journal* **9**, 333–350 (2017). <https://doi.org/10.1007/s12567-017-0167-3>
- Dupuis, P.: Highly accurate thermo-elastic distortion measurement technique for antenna reflectors. In: ecssmet (2018)
- Olivo E., Hernández, D., Garranzo, D., Barandiarán, J., Reina, M.: New environmental testing capabilities at inta. proc. In: 12th European Conference on Space Structures, Materials Environmental Testing' Noordwijk, The Netherlands, 20–23 march 2012 (esa sp-691, july 2012) (2012)
- Verlaan, A., Lucarelli, S.: Lisa telescope assembly optical stability characterization for esa. In: International Conference on Space Optics—ICSO 2014, in Proceedings (2017)
- Vaughan, M., Laine, B., Etchells, J., Rutherford, K., Bursachi, N., Kellner, M.: Correlation of a thermal model using infra-red camera data for thermo-elastic predictions. In: 50th International Conference on Environmental Systems ICES-2021–419, 11–15 July 2021 (2021)
- Prentice, E., Henriksen, M., Johansen, T., Navarro-Medina, F., San-Juan, A.: Characterizing spectral response in thermal environments, the HYPPO-1 hyperspectral imager. In: IEEE Aerospace Conference (2022)

28. Torkildsen, H.E., Skauli, T.: Measurement of point spread function for characterization of coregistration and resolution: comparison of two commercial hyperspectral cameras. In: *Algorithms and Technologies for Multispectral, Hyperspectral, and Ultraspectral Imagery XXIV*, vol. 10644, pp. 106441F. International Society for Optics and Photonics (2018)
29. Henriksen, M., Prentice, E., Maartje van Hazendonk, C., Sigernes, F., Johansen, T.: Do-it-yourself vis/nir pushbroom hyperspectral imager with c-mount optics. *Opt. Continuum* **1**, 427–441 (2022)
30. Prentice, E.F., Honoré-Livermore, E., Bakken, S., Henriksen, M.B., Birkeland, R., Hjertenæs, M., Gjersvik, A., Johansen, T.A., Aguado-Agelet, F., Navarro-Medina, F.: Pre-launch assembly, integration, and testing strategy of a hyperspectral imaging CubeSat, HYPSO-1. *Remote Sensing* **14**, 4584 (2022)
31. Gilmore, D.: *Spacecraft Thermal Control Handbook, Volume I: Fundamental Technologies*, 1st edn. The Aerospace Corporation Press, Washington DC (2002)
32. Schott: Schott optical glass collection datasheets (2018). <https://www.schott.com/en-gb/products/optical-glass-p1000267/downloads>
33. E. C. for Space Standardization, Ecss-e-hb-31-03a. *Thermal Analysis Handbook* (2016)
34. E. C. for Space Standardization, Ecss-e-st-31c – space engineering. *Thermal Control General Requirements* (2008)

Publisher's Note Springer Nature remains neutral with regard to jurisdictional claims in published maps and institutional affiliations.